

High Stability and Properties of Adsorbed Polycyclic Aromatic Hydrocarbons (PAHs) onto Phosphorene: An atomistic DFT study

*Diego Cortés-Arriagada**

Programa Institucional de Fomento a la Investigación, Desarrollo e Innovación, Universidad Tecnológica Metropolitana, Ignacio Valdivieso, 2409, San Joaquín, Santiago 8940577, Chile. *E-mail address: dcortes@utem.cl

Abstract. In this work, we report the structure, intermolecular forces, electronic/optical properties, and stability in solution of complexes formed between polycyclic aromatic hydrocarbons (PAH) and phosphorene nanoflakes by density functional theory modeling. PAH molecules reach a strong affinity with phosphorene by forming well-ordered domains, whose interaction strength decreases 13-21% compared to the interaction onto carbonaceous surfaces, e.g., graphene. The adsorption energies are in linear relation with the $N_H:N_C$ ratio of PAHs, where N_H and N_C are the numbers of H and C atoms; consequently, the cohesive energy of phosphorene-graphene heterostructures is estimated in 44 meV/atom. Energy decomposition (ALMO-EDA) and electron-density-based analyses support the major role of electrostatics driving forces in the interaction mechanism, which is balanced with dispersion effects for larger PAHs. In addition, phosphorene-PAH complexes display outstanding stability in solution under polar/non-polar solvents, which is due to the high polarity of the complexes and strong overcompensation of destabilizing solvation energies with stabilizing electrostatic effects. Moreover, PAHs behave as *n*-dopants for phosphorene, inducing small bandgap opening and weak effects on the photophysical fingerprint of phosphorene. Nevertheless, strong electron acceptor/donor and larger PAHs ($N_H:N_C < 0.5$) lead to major effects on the bandgap control, acting as active sites for orbital-controlled interactions. These findings serve as a framework for further investigation of phosphorene-based materials for remediation of PAH pollutants in water treatment technologies and uses of PAHs for phosphorene surface passivation or bandgap engineering for sensing.

Keywords: Phosphorene; adsorption; water treatment; solvent effects; graphene; interaction mechanism.

1. Introduction

Polycyclic aromatic hydrocarbons (PAHs) are an important class of non-ionic organic compounds, which have been associated with carcinogenic, mutagenic, and teratogenic behavior in humans and animals[2, 3]. Specifically, PAHs are a hazardous class of pollutants with major environmental concern, whose entering to humans over threshold values occurs through the food chain by deposition from the air or by deposition and transfer from water and soil[2, 4]. In this regard, the use of low-dimensional nanomaterials has emerged as efficient substrates for new technologies of removal, control, and remediation of PAH pollutants *via* adsorption in the solid phase[3]. For instance, graphene and its composites (e.g., coated materials, graphene oxide, reduced graphene oxide, graphene quantum dots, among others) have a large surface and π - π interaction ability that improves due to the additive character of the dispersive interactions, resulting in cost-effective adsorbents with high adsorption capacity, efficiency, and reusability [5-8]. Despite the latter, PAHs have also found application in nanotechnology; e.g., PAHs serve as non-aggressive dopant molecules to modulate the electronic properties of carbon-based materials[9-12] and assist the exfoliation of graphene flakes[13]. Moreover, a bandgap opening on the range of 102-240 meV triggered by PAHs turns graphene-based materials into semiconductors at room temperature [12, 14].

In the last years, phosphorene-based surfaces have emerged as new two-dimensional surfaces analogs to graphene. Phosphorene is a two-dimensional 2D layered system composed of phosphorous atoms interconnected by covalent sp^3 - sp^3 bonding; each atom has an in-plane covalent bond with the other two atoms and a third one out-of-plane (puckered structure), leaving a lone-electron pair. Attention on phosphorene is predominantly

attributable to its high thickness-dependent charge carrier mobility ($\sim 1000 \text{ cm}^2 \text{ V}^{-1} \text{ s}^{-1}$) and direct semiconductor monolayer bandgap of $\sim 1.5 \text{ eV}$ [15, 16]. To date, several synthetic methods have been proposed to prepare phosphorene-based materials, including ultrasonic liquid-phase exfoliation, wet-chemical, microwave-assisted synthesis, and solvothermal, top-down, and bottom-up methods [17]; therefore, their applications are expected to increase in the coming years. Remarkably, phosphorene shows an excellent adsorption ability, enhanced by a predominantly non-covalent attraction with adsorbates confirmed from experimental and theoretical methods [18-20]. In the case of PAHs, the experimental non-covalent functionalization of 2D phosphorene with boronic and azobenzene PAH derivatives results in materials with high chemical stability, promoting applications in oxygen chemosensing heterojunctions for optoelectronic and energy conversion [20, 21]. Furthermore, density functional theory studies have characterized adsorption energies on the order of 0.5-0.9 eV for molecules with aromatic rings such as phenylalanine, o-ethyltoluene, phenyl propane, DNA nucleobases, and dioxins, giving promising uses for phosphorene in pollutant removal, sensing devices, and bioinorganic interfaces [22-25].

Considering the above, the knowledge about the interaction at Phosphorene–PAHs interfaces turn into an important concern due to their useful nanotechnological applications and pollutant remediation capability. In this framework, we employed a dispersion corrected DFT methodology to obtain quantitative data related to the adsorption behavior, adsorption mechanism, and electronic/optical properties of Phosphorene–PAH complexes in the gas phase and solution.

2. Computational Methodology

We consider PAH molecules in a wide range of H:C atom ratios (N_H/N_C , 1.0–0.4) and molecular weights (78–398 g/mol): benzene (C_6H_6), naphthalene ($C_{10}H_8$), pyrene ($C_{16}H_{10}$), chrysene ($C_{18}H_{12}$), benzo[a]pyrene ($C_{20}H_{12}$), coronene ($C_{24}H_{12}$) and ovalene ($C_{32}H_{14}$). Phosphorene nanoflakes (**Phos**, $P_{126}H_{30}$) with a surface area of $\sim 1585 \text{ \AA}^2$ (considering its electron density) were used for adsorption studies, which are relatively larger to obtain well-converged adsorption energies respecting the PAHs surface ($126\text{--}371 \text{ \AA}^2$). A graphene nanoflake model (**Grap**, $C_{96}H_{26}$) was implemented for comparison purposes. DFT calculations were performed in the ORCA 4.1 program without geometry/symmetry constraints [26]. Molecular structures were optimized with the generalized gradient approximation (GGA) PBE functional combined with the all-electron def2-SVP basis sets and DFT-D3BJ dispersion correction [27–30]. All the electronic properties were obtained with the meta-GGA B97M-V functional combined with the all-electron def2-TZVP basis sets. B97M-V is a 12-parameter combinatorically-optimized functional with an electron-density based dispersion-correction from the non-local term of the VV10 functional, giving remarkable results for energetics in non-bonded interactions [31, 32]. The universal solvation model (SMD) was implemented for solvent effects, which bases on the quantum mechanical charge density of a solute molecule interacting with a continuum description of the solvent [33]. Excited states were acquired with the simplified time-dependent DFT approach combined with the meta-hybrid TPSSh functional and SMD solvent effects in *n*-hexane up to an energy threshold of 10 eV [34, 35]. Convergence tolerance values of $1 \cdot 10^{-8}$ and $1 \cdot 10^{-6}$ Ha were used for energy and geometry steps.

The stability of AB complexes was assessed by their adsorption energies (E_{ads}):

$$E_{ads}=E_{Phos}+E_{PAH}-E_{Phos-PAH} \quad (1)$$

where E_{Phos} , E_{PAH} , and $E_{Phos-PAH}$ are the total energies of the free phosphorene, free PAHs, and the AB complex, respectively; the more positive the E_{ads} values, the more stable the AB complex is. The counterpoise method was used to avoid the E_{ads} overestimation due to the basis set limit [36]. Adsorption energies were further decomposed by the energy decomposition analysis based on absolutely localized molecular orbitals (ALMO-EDA) in Q-Chem5.4 [37]. In this way, E_{ads} values are decomposed into six terms as [38, 39]:

$$-E_{ads}=\Delta E_{CT}+\Delta E_{POL}+\Delta E_{ELEC}+\Delta E_{DISP}+\Delta E_{PAULI}+\Delta E_{PREP} \quad (2)$$

where ΔE_{CT} , ΔE_{POL} , ΔE_{ELEC} , and ΔE_{DISP} stand for the energy lowering due to charge transfer (charge flow between fragments), polarization (induced electrostatics), Coulombic attractions (intermolecular electrostatics), and dispersion forces (van der Waals interactions), respectively. Destabilizing forces are accounted for by ΔE_{PAULI} (Pauli repulsion when two fragments are close enough) and ΔE_{PREP} (energy penalty due to the geometric distortion of fragments to reach the complex geometry).

Non-covalent interactions were studied with the Independent Gradient Model (IGM) [40], where the δg^{inter} index uniquely defines intermolecular interaction regions: $\delta g^{inter}=|\nabla \rho^{IGM,inter}|-|\nabla \rho|$, where $\nabla \rho$ stands for the electron density gradient and $\nabla \rho^{IGM,inter}$ is an upper limit to $\nabla \rho$ [40]. The atoms-in-molecules (AIM) method was used to obtain the electron density (ρ) at the intermolecular bond critical points (BCPs). Accordingly, covalent bonds, closed-shell interactions, and weak electrostatic interactions are characterized by ρ_i values of $\rho_i \geq 0.10$, $\rho_i \approx 0.10-0.04$, and $\rho_i \leq 0.01$ e/Bohr^3 , respectively [41]. Electron-density based analyses were performed in the Multiwfn3.8 program [42].

3. Results and discussion

3.1. Adsorption strength

For reference purposes, we computed the interlayer cohesive energy of graphite (E_{coh}), where the total adsorption energies of PAHs onto graphene (E_{ads} , Table 1) are expressed per number of carbon atoms in the PAH molecule ($E_{\text{ads}}/\text{C atom}$), which are in linear relation with the $N_{\text{H}}:N_{\text{C}}$ ratio of PAHs. The extrapolated $E_{\text{ads}}/\text{C atom}$ value at the $N_{\text{H}}:N_{\text{C}}=0$ (where PAHs turn into an infinite graphene layer) gives the estimated cohesive energy of graphite [1]. The predicted cohesive energy with the B97M-V/def2-TZVP level is $E_{\text{coh}} \approx 54.7$ meV/atom (Fig. 1a), which is in excellent agreement with the experimental reference ($E_{\text{coh}} \approx 52 \pm 5$ meV/atom) [1]. Other theoretical studies have reported E_{coh} values of 48-49 (DFT, PBE+vdW-DF), 53 meV/atom (DFT, B97-D), 43 (gCP-PBE-D3), and 52 meV/atom (force field, MMFF) [43-45]. In addition, the computed adsorption energies of benzene, naphthalene, coronene, and ovalene onto graphene are in excellent agreement with those from Redhead analyses (Table 1 in parenthesis)[1]. Consequently, the selected

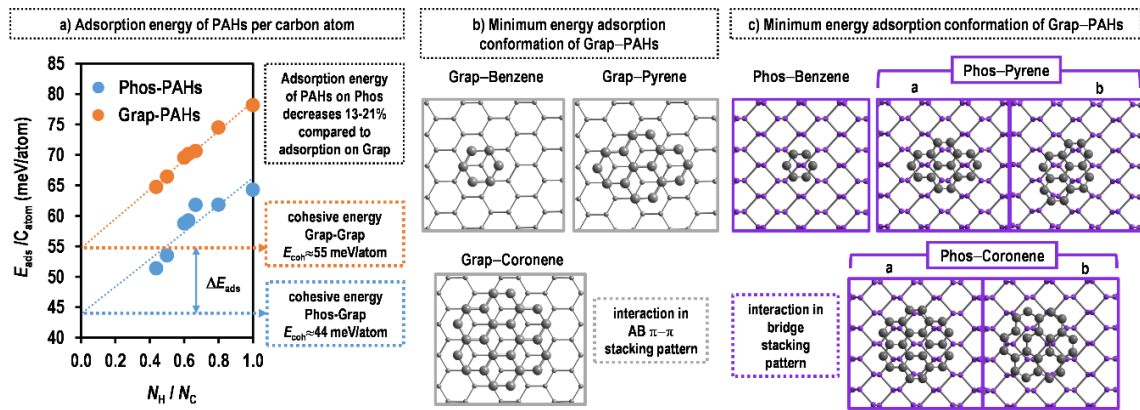


Fig. 1. a) Adsorption energy per carbon atom ($E_{\text{ads}}/\text{C atom}$) of PAHs adsorbed onto graphene (Grap) and phosphorene (Phos) according to the $N_{\text{H}}:N_{\text{C}}$ ratio of PAHs. Minimum energy structures of representative b) Grap-PAHs and c) Phos-PAHs complexes. All the adsorption configurations in the systems are in the Supplementary Material. Hydrogen atoms were deleted from the molecular representations. Color code: carbon (grey), phosphorous (purple).

methodology is adequate to study Graphene–PAH interactions and, consequently, **Phos–PAH** complexes. On the contrary, PBE-D3/def2-TZVP calculations underestimate the adsorption energies for larger PAHs, resulting in a slightly underestimated value of $E_{\text{coh}} \approx 42.1$ meV/atom as reported with agreeing with the PBE-D3/SVP method (43 meV/atom with) [46].

As a comparison, PAHs interact with graphene in A-B stacked π – π patterns^{4,40,41} (Fig. 1b); while a bridge stacking is the minim energy conformation for **Phos–PAH** complexes (relative shift of the two monolayers along the lateral direction, Fig. 1c), which is also

Table 1. Properties of Phos–PAH vs. Grap–PAH complexes: Adsorption energies (E_{ads} in eV); intermolecular distances (d_{inter} in Å); *Conf* is the code for adsorption configuration; percentage of relative occupancies (Φ , in %) of the conformations (**a-c**) at T=298 K. ^aExperimental values from Redhead analysis[1]. Φ was obtained by the Boltzmann distribution function $N_i/N_0 = e^{-(E_i - E_0)/kT}$, where N_i and N_0 are the occupancies of the i -th and the first adsorption state, while E_i and E_0 are the energies of the i -th and the first adsorption state. T and k are the absolute temperature and Boltzmann constant, respectively.

molecule	Graphene		<i>Conf</i>	Phosphorene		
	E_{ads}	d_{inter}		E_{ads}	Φ	d_{inter}
<i>benzene</i>	0.47	3.44	a	0.39	100	3.11
	(0.5+0.08) ^a					
<i>naphthalene</i>	0.75	3.50	a	0.62	69	3.13
	(0.8+0.1) ^a		b	0.60	31	3.13
<i>pyrene</i>	1.12	3.53	a	0.95	83	3.15
			b	0.91	17	3.16
<i>chrysene</i>	1.27	3.55	a	1.11	99	3.09
			b	0.93	1	3.17
			c	0.88	0	3.22
<i>benzo[a]pyrene</i>	1.39	3.55	a	1.18	99	3.19
			b	1.01	1	3.21
			c	0.96	0	3.21
<i>coronene</i>	1.59	3.56	a	1.28	100	3.25
	(1.3+0.2) ^a		b	1.14	0	3.25
<i>ovalene</i>	2.07	3.57	a	1.64	94	3.26
	(2.2+0.2) ^a		b	1.57	6	3.24
			c	1.40	0	3.29

142 allowed for graphene (with minor stability) and phosphorene-graphene non-covalent
 143 heterostructures [47-51]. Rotation of PAHs with respect to the phosphorene plane gives
 144 additional bridge stacked conformations with close stabilities (conformations **a**, **b**, or **c**, Table
 145 1). The selected PAHs interact *via* physisorption at intermolecular distances of $d_{\text{inter}}=3.1-3.3$
 146 Å from the Phos surface, which are slightly shorter compared to **Grap-PAH** complexes
 147 ($d_{\text{inter}}=3.4-3.6$); the intermolecular distances increases as the PAH molecular size increases
 148 because of the expected steric repulsion. Permanent Coulombic electrostatic forces play a
 149 key role for molecular physisorption onto phosphorene, which relates to the charge polarity
 150 in adsorbates [19, 52]; conversely, non-covalent **Grap-PAH** complexes are stabilized by the
 151 cooperative interplay between dispersion and short-range electrostatic [44, 45, 53-55]. Since
 152 unsubstituted PAHs display a weak dipole moment ($\mu_D < 0.04$ Debye) and adsorption on
 153 phosphorene are electrostatically dominated, the adsorption energy of the **Phos-PAH**
 154 complexes decreases ~13–21% compared to the adsorption onto graphene (Table 1, Fig. 1a).
 155 Despite the latter, PAHs are efficiently retained onto Phos; for instance, coronene and
 156 ovalene reach adsorption energies of up to 1.28 and 1.64 eV, respectively.

157 On the other hand, the different adsorption conformations (Fig. 1c) differ in up to
 158 ~0.14 eV among them, where the relative occupancy (Φ) of the minimum energy
 159 conformation is at least 69% at room temperature ($T=298$ K). Thus, the adsorption
 160 conformations are not energetically degenerated at room temperature, allowing PAHs to bind
 161 in well-ordered domains. Indeed, molecular dynamics and DFT simulations have shown that
 162 aromatic molecules (e.g., amino acids, benzene, porphyrins, trifluorobenzene, pentacene,
 163 trihydroxybenzene, coronene, and fullerenes) self-assemble onto phosphorene, forming two-

dimensional molecular systems with high periodicity[19, 56, 57]. Therefore, conformations with the highest stability will be considered for further analyses.

Otherwise, the extrapolation to the limit $N_H:N_C \approx 0$ provides predicted cohesive energy for non-covalent **Phos–Grap** (phosphorene-graphene) heterostructures of $E_{coh} \approx 43.9$ meV per C atom (Fig. 1a), with an intermolecular distance of ~ 3.4 Å. The reported cohesive energies of **Phos–Grap** heterostructures have a large spread, ranging from 25 to 61 meV/atom with intermolecular distances of 3.4-3.5 Å [49-51, 58, 59]. This data is a piece of valuable information because graphene-phosphorene heterostructures have opened new avenues for application in nanoelectronics, optoelectronics, 2D Dirac materials, anodes in Na/ion batteries, phosphorene protection by capping layers, and control of carrier dynamics [48-51, 58, 60, 61]. Furthermore, the adsorption energy of **Phos–PAH** complexes can be straightforwardly fitted to an empirical linear equation due to its dependence on the N_H/N_C ratio:

$$E_{ads}/\text{eV} \approx (0.065N_H + 0.028N_C - 0.170) \quad (3)$$

where N_H and N_C are the numbers of H and C atoms in PAHs, respectively. Eq. (3) provides an estimation of the adsorption energy of any neutral/non-substituted PAH adsorbed onto Phos. For example, we predicted the total adsorption energies of acenaphthene ($C_{12}H_{10}$), fluoranthene ($C_{16}H_{10}$), and fluorene ($C_{13}H_{10}$) onto phosphorene with values of 0.82, 0.93, and 0.84 eV, respectively, which are in reasonable agreement with those DFT-based E_{ads} values of 0.72, 0.89 and 0.70 eV, respectively.

3.2. Interaction Mechanism

This section aims to provide a quantitative and readily physical interpretation of the interaction mechanism. The attention is focused on the stabilizing contributions to the adsorption energies *via* relative single percentage contributions of stabilizing EDA terms (ΔE_i , Fig. 2a). Accordingly, **Phos-PAH** complexes stabilize with an almost balanced contribution from electrostatic and dispersion driving forces, similar to the physisorption of amino acids, fullerenes, and macrocyclic metal complexes [19, 52, 62]. Electrostatics forces show a slightly larger contribution (>40%) than dispersion for PAHs with a high N_H/N_C ratio ($\Delta E_{\text{ELEC}} \geq \Delta E_{\text{DISP}}$). Dispersion forces slightly exceed the electrostatic stabilization for PAHs with low N_H/N_C ratio ($\Delta E_{\text{ELEC}} \leq \Delta E_{\text{DISP}}$) because of ΔE_{ELEC} term decay more quickly when intermolecular distances increases due to its asymptotic distance dependence.

In comparison, π - π stacking of PAHs on graphene is mainly driven by dispersion forces in ~60%, while electrostatic forces contribute ~34% (Fig. 2b). Then, phosphorene is

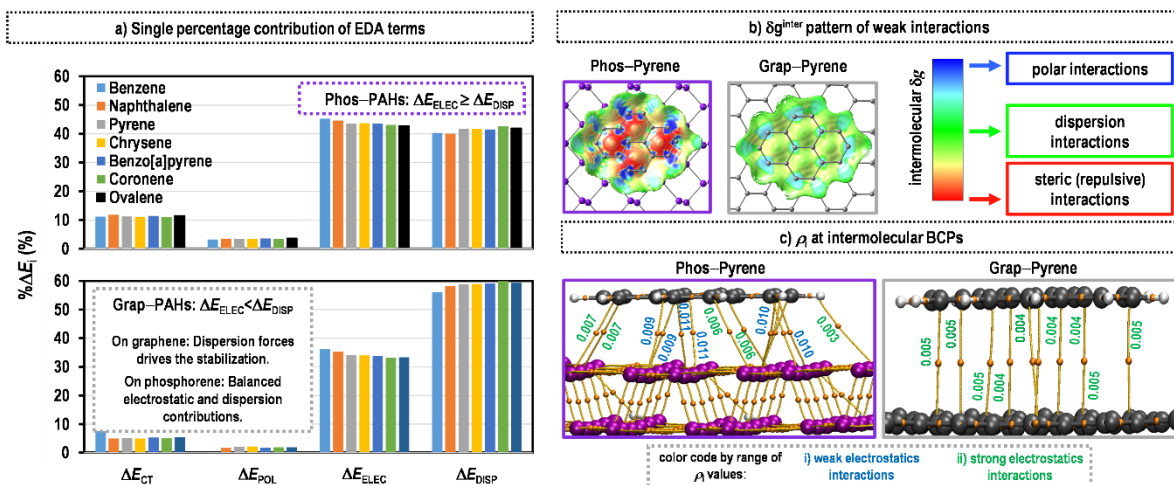


Fig. 2. a) Energy decomposition analyses of Phos-PAH and Grap-PAH complexes with the relative single percentage contributions of stabilizing EDA terms (% ΔE_i , in %). Binding analyses of representative Grap-Pyrene and Phos-Pyrene complexes: b) δg^{inter} isosurface of intermolecular interaction regions (isosurface value of 0.0003 a.u.); c) electron density at intermolecular bond critical points BCPs (ρ_i , in e/Bohr^3).

not a π -extended system, but their high number of 3p lone pair electrons at the upper lattice could correlate with the π -electrons of physisorbed aromatic systems, leading to momentary/permanent dipoles responsible for enhanced long-range effects. In this regard, the δg^{inter} isosurface plot of weak intermolecular interactions displays a comparable shape on **Phos-PAH** and **Grap-PAH** complexes, where dispersion forces play a key stabilizing effect (green regions in Fig 2b, where **Phos-Pyrene** and **Grap-Pyrene** complexes are representative cases). Nevertheless, stabilizing polar interactions are relatively higher on **Phos-PAH complexes** (blue regions), confirming the major role of electrostatic stabilization. Steric destabilization (red regions) also increases upon adsorption on phosphorene due to the high electron density coming from 3p orbitals of P atoms perpendicularly placed concerning the surface plane. In the same fashion, Fig. 2c gives the electron density values (ρ) at the intermolecular bond critical points [BCPs, points in space at which the first derivatives of the electron density vanish $\nabla\rho(r)=0$], where **Phos-Pyrene** and **Grap-Pyrene** complexes shows values of up to 0.005 and 0.011 e/Bohr^3 , respectively, which are associated with weak ($\rho\leq 0.01$ e/Bohr^3 , green numbers) or medium/strong electrostatic interactions ($\rho\geq 0.01$ e/Bohr^3 , blue numbers), respectively. Then, EDA, δg^{inter} , and AIM analyses support the major role of electrostatics stabilization on **Phos-PAH complexes**.

Otherwise, short-range charge transfer (ΔE_{CT}) and polarization (ΔE_{POL}) have minor contributions because their decays are approximately exponential to the lack of orbital overlapping (Fig. 2a). ΔE_{CT} contributes $\sim 10\%$ to the stability, which is associated with the medium electron transfer in the **PAH** \rightarrow **Phos** direction (0.1-0.2 $|e|$), and higher compared to the electron flow on **Grap-PAH** complexes ($<0.1|e|$). Fig. 3a displays the electron density

difference $[\Delta\rho(r)]$ due to charge rearrangements upon interaction, which is split into polarization and charge-transfer steps. PAHs and adsorbents mutually polarize each other at the equilibrium distances, resulting in the on-fragment density relaxation of each species to the presence of the nuclei/electrons of each fragment, inducing multipole moments that decrease as the intermolecular distances increases. Considering the **Phos-Pyrene** and **Grap-Pyrene** complexes, intramolecular charge rearrangements occur at the polarization step, accumulating electrons at the intramolecular region characterized by an energy lowering of $\Delta E_{\text{POL}} = -0.63$ and $\Delta E_{\text{POL}} = -0.19$ eV, respectively (Fig. 3a). Consequently, ΔE_{POL} has a stronger stabilizing effect in the **Phos-PAH** complexes compared to **Grap-PAHs**, which is related to the higher polarizability of phosphorene ($1.4 \cdot 4\pi\epsilon_0 \text{ \AA}^3/\text{atom}$, where ϵ_0 is the vacuum permittivity) vs. graphene ($0.5 \cdot 4\pi\epsilon_0 \text{ \AA}^3/\text{atom}$) [63, 64].

After polarization, virtual and occupied orbitals can be mixed, causing energy lowering by charge transfer. For instance, the **Grap-Pyrene** complex almost does not show

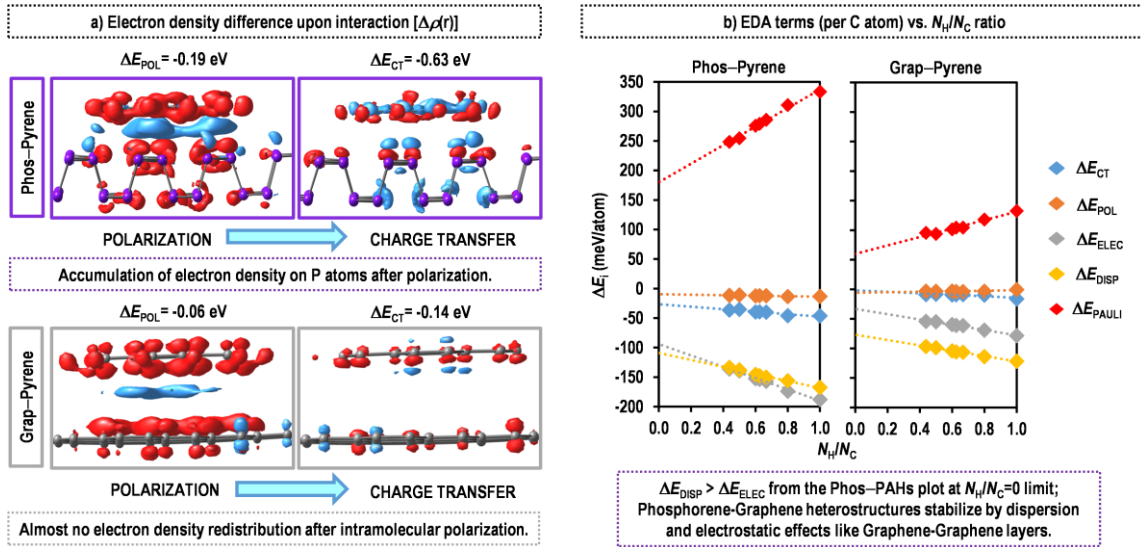


Fig. 3. a) Electron density difference $[\Delta\rho(r)]$ due to polarization and charge transfer effects in representative **Grap-Pyrene** and **Phos-Pyrene** complexes (sky-blue: increase in electron density; red: decrease in electron density). b) EDA terms (per C atom) vs. N_H/N_C ratio, and extrapolation to $N_H/N_C \approx 0$.

charge redistribution due to charge transfer (Fig. 3a), resulting in weak ΔE_{CT} stabilization (-0.06 eV); then, electron density rearrangements of **Grap-PAH** complexes is mainly due to polarization effects. Conversely, $3p$ orbitals of P atoms accumulate electron density in Phos at the charge transfer step (yellow densities), resulting in an energy lowering of $\Delta E_{CT}=-0.19$ eV. The accumulation of electron density in phosphorene also enhances the magnitude of electrostatic interactions with electron-deficient sites of PAHs (red densities).

Last but not less, extrapolation of EDA terms to the $N_H:N_C \approx 0$ limit indicates that dispersion effects surpass in $\sim 16\%$ the Coulombic interactions at **Phos-Grap** heterostructures ($\Delta E_{DISP} > \Delta E_{ELEC}$, Fig. 3b), where previous works only have highlighted the role of van der Waals forces in the stabilization [49-51, 58, 59]. Conversely, the interaction between graphene layers is always determined by dispersion forces. Remarkably, ΔE_{CT} effects also stabilize in ~ 27 meV/atom in **Phos-Grap** heterostructures, denoting a significative charge-transfer. In this regard, we estimate a charge transfer of 0.0016 electrons per C atom in the Grap \rightarrow Phos direction at the $N_H:N_C \approx 0$ limit, which agrees with values obtained from periodic DFT calculations (~ 0.0023 electrons per C atom) [49]. Finally, $\sim 99\%$ of destabilizing effects are due to Pauli repulsion (ΔE_{PAULI}) in all the systems, without larger contribution from preparation energies (ΔE_{PREP}). Then, Pauli repulsion is the main destabilizing force that compensates dispersion and electrostatic effects to determine the optimum equilibrium intermolecular distances.

3.3. Electronic properties

As previously noted, PAHs behave as mild n -dopants, acquiring a positive charge and introducing $\sim 0.1\text{--}0.2|e|$ in phosphorene per adsorbed molecule (see Q_{PAH} values, Table 2); the charge transfer decreases as the PAH size increases per number of carbon atoms ($Q_{\text{PAH}}/\text{atom}$, Table 2). The electron transfer in the PAH \rightarrow Phos direction is consistent with the electronic chemical potential (μ) of fragments (Table 2), and it relates to the electronegativity χ through $\mu = -\chi$; $\mu = (\varepsilon_{\text{HOMO}} + \varepsilon_{\text{LUMO}})/2$, where $\varepsilon_{\text{HOMO}}$ and $\varepsilon_{\text{LUMO}}$ are the eigenvalues of the HOMO and LUMO, respectively [65]. In this background, the electrons move from PAHs with high chemical potential ($\mu \geq -3.8$ eV) toward phosphorene with low chemical potential ($\mu = -4.5$ eV), giving a new electronic equilibrium. Because of the charge-transfer process, dipole moments μ_{D} of **Phos-PAH** complexes increase with respect to the non-polarized isolated fragments ($\mu_{\text{D}} \approx 0$, Table 1), denoting a decreased hydrophobicity to be stable under polar solvents. Further, the complexes show higher polarizabilities α compared to the free systems, improving the ability to acquire dipole moment under external electric fields (see α and α_{free} , Table 2).

Table 2. Electronic properties of Phos-PAHs complexes: Mulliken charge (modified by Bickelhaup) of PAHs after interaction (Q_{PAH} , in $|e|$); Q_{PAH} per number of carbons ($Q_{\text{PAH}}/\text{atom}$, in $|e|$); chemical potential (μ , in eV); dipole moment (μ_{D} , in Debye); first electric polarizability (α , in a.u.); α of isolated systems (α_{free}); HOMO and LUMO energies ($\varepsilon_{\text{HOMO}}$ and $\varepsilon_{\text{LUMO}}$), and HOMO-LUMO energy gap (Δ_{HL}).

PAH	Q_{PAH}	$Q_{\text{PAH}}/\text{atom}$	μ	μ_{D}	α	α_{free}	$\varepsilon_{\text{HOMO}}$	$\varepsilon_{\text{LUMO}}$	Δ_{HL}
<i>benzene</i>	0.06	0.011	-3.73	0.70	3455	48	-5.23	-3.69	1.55
<i>naphthalene</i>	0.10	0.010	-3.77	1.26	3479	237	-5.22	-3.66	1.57
<i>pyrene</i>	0.11	0.007	-3.76	1.04	3519	155	-5.21	-3.64	1.57
<i>chrysene</i>	0.13	0.007	-3.75	1.57	3538	471	-5.22	-3.63	1.59
<i>benzo[a]pyrene</i>	0.15	0.007	-3.78	2.10	3553	254	-5.22	-3.62	1.59
<i>coronene</i>	0.15	0.006	-3.77	2.14	3572	246	-5.17	-3.63	1.54
<i>ovalene</i>	0.19	0.006	-3.81	2.99	3636	1111	-5.06	-3.60	1.45
<i>BTQBT</i>	0.19		-3.64	2.39	3591	741	-4.85	-3.63	1.22
<i>PTCDA</i>	~ 0.00		-5.48	0.91	3611	909	-5.27	-4.56	0.70
<i>Phos</i>			-4.48	0.00		3419	-5.25	-3.72	1.53

271 Additionally, we obtained a HOMO–LUMO energy gap (Δ_{HL} , Table 2) or bandgap
 272 of 1.53 eV for intrinsic phosphorene, which is in the range of previous measurements
 273 (0.9–2.0 eV) [66–68]; HOMO and LUMO levels appear at –5.25 and –3.72 eV, respectively.
 274 PAHs induce a slight bandgap opening in phosphorene of ~10–60 meV, which is similar to
 275 the graphene bandgap opening via PAHs adsorption (~10–40 meV) [12, 69]. As an
 276 illustration, the partial density of state of the **Phos–Pyrene** complex shows that the slight
 277 bandgap opening is due to hybridization between 2p states of pyrene and phosphorene below
 278 the valence band (<–5.2 eV), which results because 2p states of PAHs are lower in energy
 279 (Fig. 4a). Consequently, the **Phos–Pyrene** complex almost does not show a contribution
 280 from pyrene to the frontier orbitals (see orbital densities in Fig 4a). Given these points,
 281 bandgap control can be achieved by larger PAHs ($N_H:N_C<0.5$) with high ionization

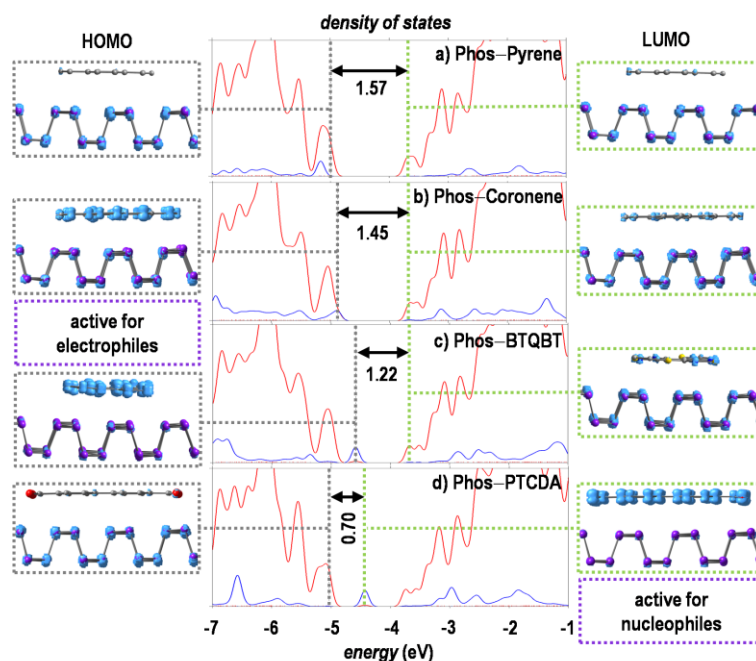


Fig. 4. a) Density of states (DOS) plots and HOMO/LUMO densities of selected Phos–PAH complexes; a) Phos–Pyrene, b) Phos–Ovalene, c) Phos–BTQBT, d) Phos–PTCDA. The grey and green lines at DOS plot indicates the position of the HOMO and LUMO level, respectively; blue and red lines are the partial DOS of the states coming from PAH and Phos, respectively. Isosurface value of 0.003 a.u.

potentials, e.g., ovalene causes a bandgap closing of ~ 90 meV because its $2p$ states hybridize with the phosphorene HOMO at the valence band, resulting in high localization of HOMO in ovalene for interaction with electrophiles (Fig. 4b). Boronic derivatives of pyrene have also resulted in a bandgap lowering by around 0.10 eV [20], while larger PAHs (near to the $N_H:N_C \approx 0$ limit) could largely affect the phosphorene bandgap due to strain effects identically to those exerted by graphene in **Phos–Grap** heterostructures [61].

It is necessary to note that a bandgap opening of up to ~ 240 meV on graphene-based substrates can be supported by the uptake of strong acceptors or donor PAHs, which control the direction/magnitude of the charge-transfer [10, 14, 69]. In the case of phosphorene, physisorption of electrophilic aromatic molecules [e.g. 3,4,9,10-perylene-tetracarboxylic-dianhydride (PTCDA), 2,3,5,6-tetrafluoro-7,7,8,8-tetracyanoquinodimethane (F4TCNQ), tetracyano-p-quinodimethane (TCNQ)] have been used to up its work function, p -type conductance, and tune the bandgap/injection barrier height [70-72]. In contrast, nucleophilic aromatics [e.g., tetrathiafulvalene (TTF)] do not cause a significant increase in the n -type semiconductor character because its donor states are far from the conduction band edge of Phos [72]. With this in mind, we characterize the adsorption of representative acceptors and donor PAHs, i.e., PTCDA and bis[1,2,5]-thiadiazolo- p -quinobis(1,3-dithiole) (BTQBT), which physisorbed onto phosphorene with adsorption energies of 1.57 and 1.13 eV, respectively, where dispersion and electrostatic forces are almost balanced like in unsubstituted PAHs ($\Delta E_{\text{ELEC}} \geq \Delta E_{\text{DISP}}$). BTQBT acts as a medium n -dopant, introducing ~ 0.2 e /molecule in phosphorene (Table 2). Due to its strong donor character, BTQBT $2p$ states hybridizes with phosphorene $3p$ states above its valence band, creating a higher HOMO level at -4.85 eV and bandgap closing of ~ 0.3 eV (Fig. 4c). For this reason, HOMO is entirely

located on BTQBT, turning the adsorbate into an active site for orbital interactions with electrophiles. On the other hand, the LUMO level of PTCDA is lower in energy compared to the LUMO of phosphorene (-4.67 eV vs. -3.72 eV); consequently, PTCDA hybridizes and creates a new unoccupied orbital near the conduction band at ~ -4.6 eV, which decrease the phosphorene bandgap in ~ 0.8 eV, avoiding the charge transfer and turning PTCDA into an active site for orbital-interactions with nucleophiles to phosphorene (Fig. 4d). In this regard, the PAHs with the electrophilic or nucleophilic activity could be implemented as signal amplifiers for specific redox applications of phosphorene. Recent studies have revealed that organic and mesoporous systems lead to signal amplification on phosphorene for outstanding sensing of polychlorinated biphenyls, hemoglobin, prostate-specific antigen, and clenbuterol, also reaching high specificity, stability, reproducibility, and low detection limits[73-75].

To establish the effects of PAHs on the photophysical fingerprint of phosphorene, it was computed the UV-Vis absorption spectrum of all the **Phos-PAH** complexes in *n*-hexane. In this regard, UV-Vis spectrophotometry measurements reveal that intrinsic phosphorene displays a wide light absorbance from the infrared region, increasing in intensity below 500 nm[76]. Then, phosphorene is photophysically active in the UV-Vis region with relatively high absorption coefficients (Fig. 5a); conversely, the studied PAHs focus the photophysical activity at the low UV region with $\lambda_{\text{abs}} < 350$ nm (Fig. 5a). In general, **Phos-PAH** complexes almost resemble the absorption profile of free phosphorene, without significant changes at higher or lower energies (Fig. 5b). This weak influence is a consequence of the lack of hybridization of PAHs with phosphorene at valence/conduction bands, resulting in a weak contribution of PAH states on HOMO and LUMO (see Fig. 4).

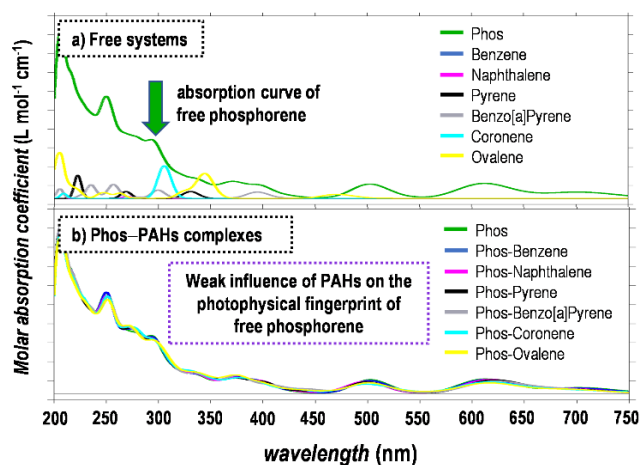


Fig. 5. Absorption spectra of a) free phosphorene and PAHs, b) Phos-PAHs complexes.

3.4. Stability in solution

With evidence about the interaction mechanisms and electronic properties, we can discuss some remarkable features of the **Phos-PAH** complexes in solution), displaying outstanding stability in different solvents and independent of the solvent polarity and molecular size (Fig. 6a). Solvation is an endergonic process in all the cases, i.e., resulting in lower adsorption energies than solvent-free calculations (Fig. 6a). Consequently, solvation energies are positives (ΔE_{SOLV}) due to the energy required to allow the solvation process; herein ΔE_{SOLV} is defined as $\Delta E_{\text{SOLV}} = E_{\text{ads}} - E_{\text{ads-solvent}}$, where $E_{\text{ads-solvent}}$ is the adsorption energy under solvation effects. As an illustration, the high polarity of the **Phos-PAHs** complexes helps its dissolution and stability on polar solvents such as water ($\epsilon \approx 78.4$, ϵ is the solvent dielectric constant) and dimethylsulfoxide ($\epsilon \approx 43.8$), where the stability decreases in $\sim 10\%$. Moreover, complexes destabilize in $\sim 18\text{-}23\%$ under solvation with medium/low polar solvents such as dichloromethane ($\epsilon \approx 8.9$) and *n*-hexane ($\epsilon \approx 1.9$), denoting that the high polarity is not high enough to avoid its stability on low-polar solvents due overcompensation of solvation destabilization from intermolecular forces.

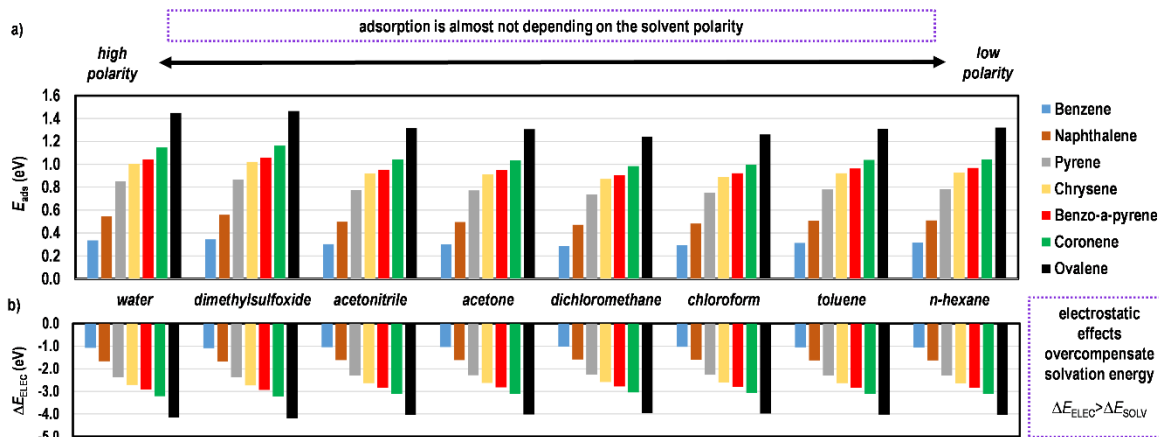


Fig. 6. a) Adsorption energies of Phos–PAH complexes in solvents (E_{ads} , in eV). b) Stabilizing electrostatic energy under different solvents (ΔE_{ELEC} , in eV).

As has been noted from EDA calculations (section 3.2), the stability of **Phos–PAH** complexes shows a strong dependence on electrostatic forces (above 40%). In this regard, ΔE_{ELEC} term in solution tracks the energy penalty due to the destabilizing solvation energies because Coulomb potential V is inversely proportional to the solvent dielectric constant (ϵ); hence, ΔE_{ELEC} contains the energy penalty due to positive ΔE_{SOLV} values in solution. Consequently, ΔE_{ELEC} energy decreases under solvation but always reaching negative values that stand for strong stabilizing or attractive effects even in solution (Fig. 6b). Therefore, electrostatic energy overcompensates all the energy penalty due to the solvation process, i.e., $\Delta E_{ELEC} > \Delta E_{SOLV}$, explaining the high stability of **Phos–PAH** complexes even under low-polar solvents such as dichloromethane and *n*-hexane as noted above.

It is important to highlight that the United States Environmental Protection Agency has selected several PAHs for monitoring, e.g., acenaphthene, acenaphthylene, fluoranthene, fluorene, naphthalene, pyrene, benzo[a]pyrene, chrysene, among others[2]. Under those circumstances, the high stability of **Phos–PAH** complexes under polar solvents indicates that

phosphorene-based adsorbents could be used to develop chemical/physical technologies to treat PAH-polluted waters. Furthermore, water molecules display weak adsorption energy to phosphorene ($\sim 80\text{--}180$ meV/molecule) [77, 78]; therefore, water molecules can be easily replaced by PAH molecules upon co-adsorption, where the displacement efficiency can be regulated by oxygen-containing groups as established for graphene nanoadsorbents [5]. In these cases, the effect of pH on the adsorption stability is almost negligible due to the lack of functional groups in PAHs [79].

On the other hand, phosphorene-layered materials can be oxidized underwater, and aerobic conditions, and new synthetic techniques are developed to improve their stability for future technologies [77]. In this regard, interaction with organic systems (e.g., C_{60} fullerenes, hexamethylenediamine, linear alkanes) and Phos/MXene (Ti_3C_2) heterostructures in air-water interfaces help to protect phosphorene thin films from oxidation when they were exposed to air and water, retaining their original form and inhibiting the agglomeration of phosphorene nanosheets in solvents [73, 80-82]. In this way, the strong PAHs physisorption could be implemented as non-covalent protective molecules for phosphorene passivation techniques, allowing further functionalization for specific technological uses. Specifically, medium size PAHs are excellent candidates for such application ($N_H/N_C \approx 0.5$), mainly because they almost retain the electronic properties of the substrate, i.e., causing weak changes in the bandgap and photophysical signature of intrinsic phosphorene. Note that molecular passivation techniques of phosphorene have also allowed increasing its sensitivity, selectivity, and flexibility for toxic gaseous detection and biosensing[83, 84].

4. Conclusions

Using a first-principles strategy, we have concluded that non-ionic/unsubstituted PAHs reach a strong affinity with phosphorene, which decreases 13-21% compared to the interaction strength with graphene. The reached adsorption can be expressed as $E_{ads}/\text{eV} \approx (0.065N_H + 0.028N_C - 0.170)$, where N_H and N_C are the number of H and C atoms in PAHs, respectively. In this way, the cohesive energy of **Phos–Grap** heterostructures is estimated in 44 meV/atom. ALMO-EDA, δg^{inter} , and AIM analyses support the major role of electrostatics interactions upon adsorption on phosphorene, balanced with dispersion forces as the $N_H:N_C$ ratio of PAHs decreases (larger size). Moreover, PAHs behave as *n*-dopants but inducing small bandgap openings ($\sim 10\text{--}60$ meV) and weak effects on the photophysical fingerprint of phosphorene. However, strong acceptor/donor and larger PAHs ($N_H:N_C < 0.5$) lead to major effects on the bandgap control. Finally, **Phos–PAH** complexes display outstanding stability in different solvents and are independent of the solvent polarity, which is favored by the high polarity and strong overcompensation of solvation energies due to electrostatic effects. Our findings suggest a framework for further investigating phosphorene-based materials for remediation of PAH pollutants, phosphorene surface passivation, or bandgap engineering.

Acknowledgments

The authors thank the financial support and computational resources through projects ANID FONDECYT/Regular 1210355 and ANID-FONDEQUIP EQM180180. Powered@NLHPC: This research was partially supported by the supercomputing infrastructure of the NLHPC (ECM-02).

403 **References**

- 404 [1] R. Zacharia, H. Ulbricht, T. Hertel, *Phys. Rev. B* 69 (2004) 155406.
- 405 [2] Z. Zelinkova, T. Wenzl, *Polycyclic Aromat. Compd.* 35 (2015) 248.
- 406 [3] A.O. Adeola, P.B.C. Forbes, *Water Environ. Res.* 93 (2021) 343.
- 407 [4] I. Tongo, O. Ogbeide, L. Ezemonye, *Toxicol. Rep.* 4 (2017) 55.
- 408 [5] K. Yang, B. Chen, L. Zhu, *Sci. Rep.* 5 (2015) 11641.
- 409 [6] A.O. Adeola, P.B.C. Forbes, *Environ. Technol.* (2020) 1.
- 410 [7] H. Hsu, C. Kuo, J. Jehng, C. Wei, C. Wen, J. Chen, L. Chen, *J. Environ. Chem. Eng.* 7
- 411 (2019) 103414.
- 412 [8] X. Gan, Y. Teng, W. Ren, J. Ma, P. Christie, Y. Luo, *Pedosphere* 27 (2017) 527.
- 413 [9] J. Zhao, J.P. Lu, J. Han, C.-K. Yang, *Appl. Phys. Lett.* 82 (2003) 3746.
- 414 [10] S.M. Kozlov, F. Viñes, A. Görling, *Carbon* 50 (2012) 2482.
- 415 [11] H.Y. Mao, Y.H. Lu, J.D. Lin, S. Zhong, A.T.S. Wee, W. Chen, *Prog. Surf. Sci.* 88 (2013)
- 416 132.
- 417 [12] D.-M. Chen, P.M. Shenai, Y. Zhao, *Phys. Chem. Chem. Phys.* 13 (2011) 1515.
- 418 [13] X. Dong, Y. Shi, Y. Zhao, D. Chen, J. Ye, Y. Yao, F. Gao, Z. Ni, T. Yu, Z. Shen, *Phys.*
- 419 *Rev. Lett.* 102 (2009) 135501.
- 420 [14] S.M. Kozlov, F. Viñes, A. Görling, *Adv. Mater.* 23 (2011) 2638.
- 421 [15] M. Wu, X. Qian, J. Li, *Nano Lett.* 14 (2014) 5350.
- 422 [16] J. Qiao, X. Kong, Z.-X. Hu, F. Yang, W. Ji, *Nat. Commun.* 5 (2014) 4475.
- 423 [17] K.N. Dinh, Y. Zhang, W. Sun, *JPhys Energy* 3 (2021) 032007.
- 424 [18] D. Cortés-Arriagada, D.E. Ortega, *J. Mol. Liq.* 307 (2020) 112958.
- 425 [19] D. Cortés-Arriagada, S. Miranda-Rojas, F. Cid-Mora, A. Toro-Labbé, *J. Mol. Liq.* 333
- 426 (2021) 115948.
- 427 [20] M. Bolognesi, S. Moschetto, M. Trapani, F. Prescimone, C. Ferroni, G. Manca, A. Ienco,
- 428 S. Borsacchi, M. Caporali, M. Muccini, M. Peruzzini, M. Serrano-Ruiz, L. Calucci, M.A.
- 429 Castriciano, S. Toffanin, *ACS Appl. Mater. Interfaces* 11 (2019) 22637.
- 430 [21] D. Zheng, M. Ding, Y. Hu, J. Zhao, C. Liu, X. Li, P. Liu, Z. Jin, J. Ma, *J. Phys. Chem.*
- 431 *C* 124 (2020) 15961.
- 432 [22] P. Rubio-Pereda, G. H. Coccoletzi, *Appl. Surf. Sci.* 427 (2018) 1227.
- 433 [23] V. Nagarajan, R. Chandiramouli, *J. Mol. Liq.* 326 (2021) 115320.
- 434 [24] D. Cortés-Arriagada, *J. Phys. Chem. C* 122 (2018) 4870.
- 435 [25] H.-p. Zhang, J.-l. Hou, Y. Wang, P.-p. Tang, Y.-p. Zhang, X.-y. Lin, C. Liu, Y. Tang,
- 436 *Chemosphere* 185 (2017) 509.
- 437 [26] F. Neese, *Wiley Interdiscip. Rev.: Comput. Mol. Sci.* 8 (2018) e1327.
- 438 [27] J.P. Perdew, K. Burke, Y. Wang, *Phys. Rev. B* 54 (1996) 16533.
- 439 [28] F. Weigend, R. Ahlrichs, *Phys. Chem. Chem. Phys.* 7 (2005) 3297.
- 440 [29] S. Grimme, J. Antony, S. Ehrlich, H. Krieg, *J. Chem. Phys.* 132 (2010) 154104.
- 441 [30] S. Grimme, S. Ehrlich, L. Goerigk, *J. Comput. Chem.* 32 (2011) 1456.
- 442 [31] N. Mardirossian, M. Head-Gordon, *J. Chem. Phys.* 142 (2015) 074111.
- 443 [32] D. Manna, M.K. Kesharwani, N. Sylvestsky, J.M.L. Martin, *J. Chem. Theory Comput.*
- 444 13 (2017) 3136.
- 445 [33] A.V. Marenich, C.J. Cramer, D.G. Truhlar, *J. Phys. Chem. B* 113 (2009) 6378.
- 446 [34] C. Bannwarth, S. Grimme, *Comput. Theor. Chem.* 1040-1041 (2014) 45.
- 447 [35] V.N. Staroverov, G.E. Scuseria, J. Tao, J.P. Perdew, *J. Chem. Phys.* 119 (2003) 12129.

448 [36] S.F. Boys, F.d. Bernardi, *Mol. Phys.* 19 (1970) 553.

449 [37] Y. Shao, Z. Gan, E. Epifanovsky, A.T.B. Gilbert, M. Wormit, J. Kussmann, A.W. Lange,

450 A. Behn, J. Deng, X. Feng, D. Ghosh, M. Goldey, P.R. Horn, L.D. Jacobson, I. Kaliman,

451 R.Z. Khaliullin, T. Kuš, A. Landau, J. Liu, E.I. Proynov, Y.M. Rhee, R.M. Richard, M.A.

452 Rohrdanz, R.P. Steele, E.J. Sundstrom, H.L. Woodcock, P.M. Zimmerman, D. Zuev, B.

453 Albrecht, E. Alguire, B. Austin, G.J.O. Beran, Y.A. Bernard, E. Berquist, K. Brandhorst,

454 K.B. Bravaya, S.T. Brown, D. Casanova, C.-M. Chang, Y. Chen, S.H. Chien, K.D. Closser,

455 D.L. Crittenden, M. Diedenhofen, R.A. DiStasio, H. Do, A.D. Dutoi, R.G. Edgar, S. Fatehi,

456 L. Fusti-Molnar, A. Ghysels, A. Golubeva-Zadorozhnaya, J. Gomes, M.W.D. Hanson-Heine,

457 P.H.P. Harbach, A.W. Hauser, E.G. Hohenstein, Z.C. Holden, T.-C. Jagau, H. Ji, B. Kaduk,

458 K. Khistyayev, J. Kim, J. Kim, R.A. King, P. Klunzinger, D. Kosenkov, T. Kowalczyk, C.M.

459 Krauter, K.U. Lao, A.D. Laurent, K.V. Lawler, S.V. Levchenko, C.Y. Lin, F. Liu, E. Livshits,

460 R.C. Lochan, A. Luenser, P. Manohar, S.F. Manzer, S.-P. Mao, N. Mardirossian, A.V.

461 Marenich, S.A. Maurer, N.J. Mayhall, E. Neuscamman, C.M. Oana, R. Olivares-Amaya,

462 D.P. O'Neill, J.A. Parkhill, T.M. Perrine, R. Peverati, A. Prociuk, D.R. Rehn, E. Rosta, N.J.

463 Russ, S.M. Sharada, S. Sharma, D.W. Small, A. Sodt, T. Stein, D. Stück, Y.-C. Su, A.J.W.

464 Thom, T. Tsuchimochi, V. Vanovschi, L. Vogt, O. Vydrov, T. Wang, M.A. Watson, J.

465 Wenzel, A. White, C.F. Williams, J. Yang, S. Yeganeh, S.R. Yost, Z.-Q. You, I.Y. Zhang,

466 X. Zhang, Y. Zhao, B.R. Brooks, G.K.L. Chan, D.M. Chipman, C.J. Cramer, W.A. Goddard,

467 M.S. Gordon, W.J. Hehre, A. Klamt, H.F. Schaefer, M.W. Schmidt, C.D. Sherrill, D.G.

468 Truhlar, A. Warshel, X. Xu, A. Aspuru-Guzik, R. Baer, A.T. Bell, N.A. Besley, J.-D. Chai,

469 A. Dreuw, B.D. Dunietz, T.R. Furlani, S.R. Gwaltney, C.-P. Hsu, Y. Jung, J. Kong, D.S.

470 Lambrecht, W. Liang, C. Ochsenfeld, V.A. Rassolov, L.V. Slipchenko, J.E. Subotnik, T. Van

471 Voorhis, J.M. Herbert, A.I. Krylov, P.M.W. Gill, M. Head-Gordon, *Mol. Phys.* 113 (2015)

472 184.

473 [38] P.R. Horn, Y. Mao, M. Head-Gordon, *Phys. Chem. Chem. Phys.* 18 (2016) 23067.

474 [39] P.R. Horn, Y. Mao, M. Head-Gordon, *J. Chem. Phys.* 144 (2016) 114107.

475 [40] C. Lefebvre, G. Rubez, H. Khartabil, J.-C. Boisson, J. Contreras-García, E. Hénon, *Phys.*

476 *Chem. Chem. Phys.* 19 (2017) 17928.

477 [41] A. Becke, C.F. Matta, R.J. Boyd, *The quantum theory of atoms in molecules: from solid*

478 *state to DNA and drug design.* John Wiley & Sons, 2007.

479 [42] T. Lu, F. Chen, *J. Comput. Chem.* 33 (2012) 580.

480 [43] J. Antony, B. Alameddine, T.A. Jenny, S. Grimme, *J. Phys. Chem. A* 117 (2013) 616.

481 [44] J. Björk, F. Hanke, C.-A. Palma, P. Samori, M. Cecchini, M. Persson, *J. Phys. Chem.*

482 *Lett.* 1 (2010) 3407.

483 [45] W. Wang, Y. Zhang, Y.-B. Wang, *J. Chem. Phys.* 140 (2014) 094302.

484 [46] J.G. Brandenburg, M. Alessio, B. Civalieri, M.F. Peintinger, T. Bredow, S. Grimme, *J.*

485 *Phys. Chem. A* 117 (2013) 9282.

486 [47] K.-G. Zhou, H.-L. Zhang, *Kirk-Othmer Encyclopedia of Chemical Technology*, p. 1-21.

487 [48] X. Dai, L. Zhang, Y. Jiang, H. Li, *Ceram. Int.* 45 (2019) 11584.

488 [49] Y. Cai, G. Zhang, Y.-W. Zhang, *J. Phys. Chem. C* 119 (2015) 13929.

489 [50] W. Hu, T. Wang, J. Yang, *J. Mater. Chem. C* 3 (2015) 4756.

490 [51] B. Liu, L.-J. Wu, Y.-Q. Zhao, L.-Z. Wang, M.-Q. Cai, *Phys. Chem. Chem. Phys.* 18

491 (2016) 19918.

492 [52] D. Cortés-Arriagada, D.E. Ortega, *Carbon* 182 (2021) 354.

493 [53] Y. Wang, Z. Xu, Y.N. Moe, *Chem. Phys.* 406 (2012) 78.

494 [54] Y. Hsun Su, Y. Kai Wu, S.L. Tu, S.-J. Chang, *Appl. Phys. Lett.* 99 (2011) 163102.

- [55] B. Bhattacharya, U. Sarkar, N. Seriani, *J. Phys. Chem. C* 120 (2016) 26579.
- [56] T.K. Mukhopadhyay, A. Datta, *J. Phys. Chem. C* 121 (2017) 10210.
- [57] T. Gorkan, Y. Kadioglu, E. Aktürk, S. Ciraci, *Phys. Chem. Chem. Phys.* 22 (2020) 26552.
- [58] H.V. Phuc, V.V. Ilyasov, N.N. Hieu, C.V. Nguyen, *Vacuum* 149 (2018) 231.
- [59] J.E. Padilha, A. Fazzio, A.J.R. da Silva, *Phys. Rev. Lett.* 114 (2015) 066803.
- [60] H.W. Lee, H. Jung, B.C. Yeo, D. Kim, S.S. Han, *J. Phys. Chem. C* 122 (2018) 20653.
- [61] X.-R. Hu, J.-M. Zheng, Z.-Y. Ren, *Front. Phys.* 13 (2017) 137302.
- [62] M. Khavani, M. Izadyar, S. Samadian, *J. Mol. Liq.* (2021) 116865.
- [63] P. Kumar, B.S. Bhadoria, S. Kumar, S. Bhowmick, Y.S. Chauhan, A. Agarwal, *Phys. Rev. B* 93 (2016) 195428.
- [64] E.K. Yu, D.A. Stewart, S. Tiwari, *Phys. Rev. B* 77 (2008) 195406.
- [65] P. Geerlings, F. De Proft, W. Langenaeker, *Chem. Rev.* 103 (2003) 1793.
- [66] A. Castellanos-Gomez, *J. Phys. Chem. Lett.* 6 (2015) 4280.
- [67] B. Van Troeye, A. Lherbier, J.-C. Charlier, X. Gonze, *Phys. Rev. Mater.* 2 (2018) 074001.
- [68] N. Saikia, M. Seel, R. Pandey, *J. Phys. Chem. C* 120 (2016) 20323.
- [69] C.-H. Chang, X. Fan, L.-J. Li, J.-L. Kuo, *J. Phys. Chem. C* 116 (2012) 13788.
- [70] C. Wang, D. Niu, B. Liu, S. Wang, X. Wei, Y. Liu, H. Xie, Y. Gao, *J. Phys. Chem. C* 121 (2017) 18084.
- [71] Y. He, F. Xia, Z. Shao, J. Zhao, J. Jie, *J. Phys. Chem. Lett.* 6 (2015) 4701.
- [72] R. Zhang, B. Li, J. Yang, *J. Phys. Chem. C* 119 (2015) 2871.
- [73] S. Liang, L. Wu, H. Liu, J. Li, M. Chen, M. Zhang, *Biosens. Bioelectron.* 126 (2019) 30.
- [74] H. Liang, H. Xu, Y. Zhao, J. Zheng, H. Zhao, G. Li, C.-P. Li, *Biosens. Bioelectron.* 144 (2019) 111691.
- [75] X. Li, X. Niu, W. Zhao, W. Chen, C. Yin, Y. Men, G. Li, W. Sun, *Electrochem. Commun.* 86 (2018) 68.
- [76] H. Liu, P. Lian, Q. Zhang, Y. Yang, Y. Mei, *Electrochem. Commun.* 98 (2019) 124.
- [77] G. Wang, W.J. Slough, R. Pandey, S.P. Karna, *2D Mater.* 3 (2016) 025011.
- [78] Y. Xu, W. Guo, *J. Alloys Compd.* 737 (2018) 365.
- [79] A.O. Adeola, P.B.C. Forbes, *Water Sci. Technol.* 80 (2020) 1931.
- [80] H. Li, P. Lian, Q. Lu, J. Chen, R. Hou, Y. Mei, *Mater. Res. Express* 6 (2019) 065504.
- [81] J. Mao, O. Ortiz, J. Wang, A. Malinge, A. Badia, S. Kéna-Cohen, *Nanoscale* 12 (2020) 19814.
- [82] A. Lorenzoni, M. Baldoni, E. Besley, F. Mercuri, *Phys. Chem. Chem. Phys.* 22 (2020) 12482.
- [83] Y. Tang, K. Yang, Z. Hua, F. Yin, W. Yuan, *Sens. Actuators, B* 329 (2021) 129233.
- [84] A. Kumar, *ACS Appl. Nano Mater.* 2 (2019) 2397.